Journal of Engg. Research Vol. 7 No. (2) June 2019 pp. 210-225

Extended targets modelling and block agnostic sparse reconstruction in through-the-wall radar imaging: A different perspective

Abdi T. Abdalla*, Mohammad T. Alkhodary** and Ali H. Muqaibel***

**University of Dar es Salaam, Electronics and Telecommunications Engineering Department, Dar es Salaam, Tanzania*
***École de Technologie Supérieure, Montréal, QC, Canada*
****King Fahd University of Petroleum and Minerals, Electrical Engineering Department, Dhahran, Saudi Arabia, 31261*
***Corresponding Author: mohammad.alkhodary.1@ens.etsmtl.ca*

ABSTRACT

A common target model in through-the-wall radar (TWRI) imaging literature obeys the point target (PT) assumption in which a target is hypothesized to occupy a single pixel. Unlike PTs, the received signal reflected from extended target (ET) is an integration of the scattered signals from various parts of the same target. For high resolution images, a generalized model is needed to encompass the ETs. In this paper, we suggest a different but realistic ET reconstruction approach based on agnostic block sparsity. The algorithm does not impose any assumption on the length, number, or the distribution of the blocks. Results based on MATLAB simulation and experimental data show the effectiveness of the proposed reconstruction approach. The applications of the suggested approach are found in civil, rescue, surveillance, and security enforcement sectors, where an accurate tracking of large targets behind walls is vital.

INTRODUCTION

The objective of through-the-wall radar imaging (TWRI) is to acquire highly resolved images of obscured areas using electromagnetic (EM) waves. TWRI is increasingly useful in determining building interiors, rescuing people in case of fire or earthquakes, and undergoing law enforcement (Amin, *et al*., 2013). This technology has witnessed a tremendous growth and attracted the attention of many researchers in the last few years (Alkhodary *et al*., 2018; Muqaibel *et al*., 2017; Muqaibel *et al*., 2017).

TWRI signals can be generated by either transmitting an ultra-short pulse or a series of step-frequencies that cover a wide band. The former is known as the time-domain impulse radar, and the latter is the step-frequency continuous wave (SFCW) radar (Gurbuz *et al.,* 2009; Huang *et al.,* 2010; Muqaibel *et al.,* 2017; Nicolaescu *et al.,* 2003). Transmitting an ultra-short pulse requires extremely fast and complex A/D converters at the receiver. In contrast, SFCW measures only the amplitude and the phase of the received frequencies, which leads to a simple design of the receiver. In addition, SFCW has relatively high noise immunity, which is adopted in this work.

Unlike in point targets (PTs), the received signal from extended target (ET) is an integration of the scattered signals from various parts of the same target (Alkhodary *et al.,* 2017). Point target is presented as a single pixel in the radar image, while ET is represented by collection of adjacent pixels in the image. In most TWRI applications, targets are more likely to be ET; as such, a more generalized model is needed to encompass the ETs as the previous point-like assumption does not hold. This clustering of the target pixels can be exploited to enhance the reconstruction performance (Eldar *et al.,* 2010; Masood *et al.,* 2013b; Wu *et al.,* 2015).

The ET is described using two parameters: the target length and the target reflection coefficient (Gennarelli *et al.,* 2015; Yoon *et al.,* 2008). In the literature, two types of reflection coefficients' distributions have been considered: assuming constant value distribution across the entire target extent and the spatial-Gaussian distribution (Yoon *et al.,*

2008). The constant value coefficient implies that the energy of the reflected signal across the entire target is the same. On the other hand, the spatial-Gaussian distributed coefficients imply that the energy of the reflected signal is most pronounced at the center of the targets (Wu *et al.,* 2008). However, the two assumptions do not apply in wide range of real TWRI applications and we, therefore, claim in this work that it is fair and realistic to assume unknown distribution for the reflection coefficients, i.e., *target agnostic* instead.

To the best of the authors' knowledge, ET modeling with sparse reconstruction in TWRI has not been rigorously studied or modeled yet. A few recent contributions on ETs under CS are available (Lagunas, 2014; Leigsnering *et al.,* 2011; Zhang *et al.,* 2015). For the CS-based reconstruction, there are two main suggested approaches to deal with ETs, which are wavelet decomposition (Leigsnering *et al.,* 2011) and uniform block sparsity approaches (Lagunas, 2014). A contribution based on wavelet transform alluded that the wavelet transform did not bode well following the challenges of the transform (Leigsnering *et al.,* 2011). On the other hand, Lagunas (2014) proposed block sparsity as a solution to the ET problem. The author suggested the use of block sparse reconstruction algorithm mentioning a block orthogonal matching pursuit (BOMP) (Eldar *et al.,* 2010) as a possible candidate. In Wu *et al.* (2015) the authors exploited the group sparsity due to the multi-polarization sensing modality, and the clustering sparsity due to the target spatial extent using modified clustered multi-task Bayesian compressive sensing. These proposals are only applicable for rectangular shaped targets, because after vectorizing the 2D image to 1D image, the block will be dissembled to consecutive pixels in the 1D image with equal length. This scenario is treated as "block sparse" scheme. In real TWRI applications, we are dealing with more complex targets like humans, rifles, to name a few, whose shapes cannot be well approximated by rectangular shapes. This calls for a more generalized model.

Unlike convex-optimization-based and greedy algorithms, Bayesian-based algorithms capitalize on the statistical information of the signal to enhance reconstructions (Sun *et al.,* 2016; Zhang *et al.,*2015; Zhang *et al.*, 2012). This has granted Bayesian-based algorithms superiority over others. Several Bayesian-based algorithms were developed to tackle the block-sparsity signals as in Zhang *et al.,* 2012; Zhang, 2012. Nevertheless, they imposed some conditions on the distribution of the non-zero pixels and on the block-size, which might be impractical for some applications (Masood *et al.,* 2013a). For instance, in TWRI applications, the target's size, shape, and their reflectivity distributions are unknown a priori.

In light of the above, the appropriate reconstruction algorithm in TWRI is desired to minimize error in image reconstruction, work under different block shapes and sizes, and unknown target distribution of the target reflectivity.

In this paper, we suggest a new ET reconstruction approach that is agnostic to the target's shape, size, and reflectivity distribution, which best mimic the TWRI scenarios. The signal model is formed so that it describes the ground truth and may appear as block sparse vectors with unknown block sizes and unknown target distributions. The variation of the block sizes in the image vector reflects complex shaped target of the ground truth.

The additional advantage of the proposed model is that if the scene comprises a mixture of PTs and ETs, it can reconstruct both concurrently by treating PTs as blocks of one size, contrary to the existing approaches where the two are reconstructed independently as in Yoon *et al.,* 2008.

The remainder of the paper is organized as follows: Section 2 introduces the received signal model. The agnostic block sparse reconstruction is presented in Section 3. In Section 4, the performance metrics used are highlighted. The normalized mean-squared error and earth mover's distance are defined. Sections 5 and 6 contain the results discussion and concluding remarks, respectively.

RECEIVED SIGNAL MODEL

In this section, an ET signal model for 2D imaging is deduced. An example of an ET, which extends in both range and crossrange directions, is depicted in Fig 1 (a) and its corresponding 1D vectorized scene is depicted in Fig 1 (b). The distribution of the pixel intensity distribution is assumed to be unavailable a priori. The assumption is justifiable

in TWRI applications as in multiple target scenarios the ground truth, which is obtained by concatenating columns of the scene matrix, may have complicated reflectivity distributions.

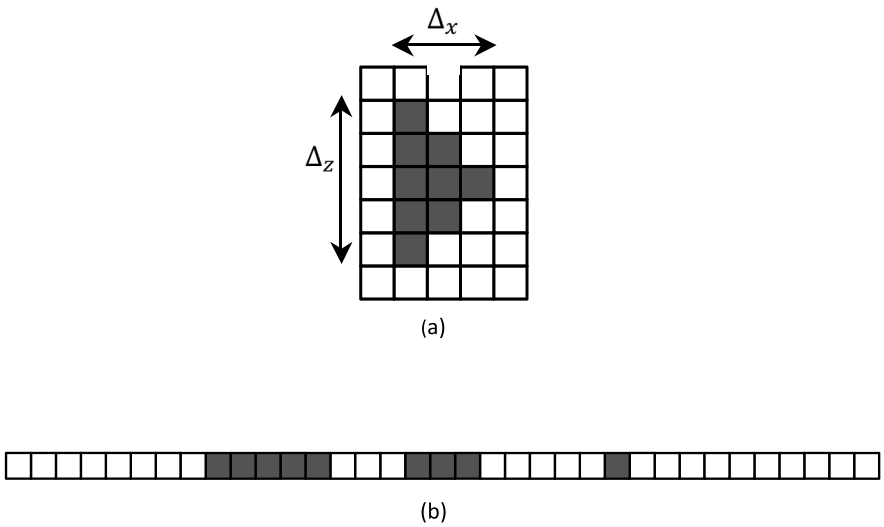

Fig. 1. Block representation of extended signal: (a) the original scene (b) vectorized scene.

Consider a synthetic aperture radar (SAR) system of N locations, which transmits at each location M equally spaced monochromatic signal for the scene interrogation. The target is assumed to span an area of Δx by Δz. The total return at the n^{th} radar location due to Q ETs when the m^{th} frequency, f_m, is transmitted can be expressed as

$$y[m,n] = \sum_{q=0}^{Q-1} \int_0^{\Delta_{qz}} \int_0^{\Delta_{qx}} \sigma_{q_{xz}} exp(-j2\pi f_m \tau_{xzn}) dxdz + y_w(m,n) + v(m,n) \qquad (1)$$

where $\sigma_{q_{xz}}$ is the reflectivity of the point (x,z) laying on the q^{th} target and τ_{xzn} is its corresponding delay and $y_w(m,n)$ is the contribution from the front wall.

For highly resolved images, the scene is subdivided into small sized pixels along the crossrange and downrange. If N_x and N_y represent the number of pixels in crossrange and downrange, respectively, then the response in (1) can be expressed as

$$y[m,n] = \sum_{q=0}^{Q-1} \sum_{p=0}^{N_x N_y - 1} \sigma_{pq} \exp\left(-j2\pi f_m \tau_{pn}\right) + y_w(m,n) + v(m,n) \qquad (2)$$

where σ_{pq} refers to the reflectivity of the p^{th} pixel laying on the q^{th} target. For mathematical simplification, we model the scene as the sum of disjoint ground truths assuming each target is coming from a different scene. In matrix form, we can write (2) as

$$\mathbf{y} = \mathbf{\Psi}\boldsymbol{s}_1 + \mathbf{\Psi}\boldsymbol{s}_2 + \cdots + \mathbf{\Psi}\boldsymbol{s}_{Q-1} + \mathbf{\Psi}\mathbf{s}_{\mathrm{w}} + \mathbf{v} = \mathbf{\Psi}\mathbf{s} + \mathbf{v}$$

$$\mathbf{s} = \mathbf{s}_0 + \mathbf{s}_1 + \cdots + \mathbf{s}_{Q-1} + \boldsymbol{s}_w \qquad (3)$$

$\mathbf{y} = (y[0,0], y[1,0], \ldots y[M-1,0], y[0,1], \ldots\ y[M-1, N-1])^T$, $\mathbf{s}_q \in \mathbb{C}^{\boldsymbol{N_x N_y \times 1}}$, is a vector of reflectivities, σ_{pq} of the q^{th} ground truth, $\boldsymbol{s}_w$ is the vector of reflectivities representing the front wall and the entries of the matrix $\mathbf{\Psi} \in \mathbb{C}^{MN \times N_x N_y}$ are defined as (Abdalla, *et al.,* 2015)

$$[\boldsymbol{\Psi}]_{ip} = \exp\left(-j2\pi f_m \tau_{pn}\right)$$
$$m = i \bmod M, \qquad n = \left\lfloor \frac{i}{M} \right\rfloor, \qquad i = 1,2,..MN-1 \tag{4}$$

Analogous to Masood (2015), $\mathbf{s}$ can be further modeled as Hadamard product, $\boldsymbol{s} = \boldsymbol{s}_A \odot \boldsymbol{s}_B$, where $\boldsymbol{s}_A$ is the vector of target's reflectivity values with unknown distribution and $\boldsymbol{s}_B$ is the binary vector with Bernoulli's distribution indicating the presence or absence of a given target pixel.

When the ground truth, $\mathbf{s}$, comprises Q independent and complex shaped ETs, is discretized, and then is vectorized by appending its columns, it results in a tall vector with K active blocks of varying length and varying probability density functions (pdf). The pdf of the k^{th} block in $\boldsymbol{s}_A$, f_{s_k} is not necessarily equal to f_{sj}, for $k \neq j$. Since the chunks of pixels are disjoint, then the probability distribution of the overall vector $\boldsymbol{s}_A$, f_s is given by

$$f_s = \begin{cases} f_{s_1} & 0 < x < x_0 \\ f_{s_2} & x_0 < x < x_1 \\ \vdots & \vdots \\ f_{s_K} & x_{K-1} < x < x_K \end{cases} \tag{5}$$

$$f_s = \sum_{k=1}^{K} f_{s_k} \times [u(x_k - x_{k-1})]$$

where $|x_{k-1} - x_k|$ signifies the k^{th} block size, which is not necessarily the same for different values of k. Equation (5) asserts that even if the distribution of each target is known, the overall distribution of the vectorized scene is not straight forward. Therefore, it is impractical to assume a particular distribution on the pixels' value as in many Bayesian-based algorithms. In the following section, we show how the developed algorithm is agnostic to the distribution of the pixels' values.

BLOCK SPARSE IMAGE RECONSTRUCTION

Equation (3) uses the full data sample; however , and since image vector, $\mathbf{s}$, is sparse, we can use the concept of CS to take compressed measurements using the matrix $\boldsymbol{\Phi}$. Define the compressed observation vector, $\bar{\mathbf{y}}$, as

$$\bar{\mathbf{y}} = \boldsymbol{\Phi}\boldsymbol{\Psi}\,\mathbf{s} + \bar{\mathbf{v}} = \mathbf{D}\mathbf{s} + \bar{\mathbf{v}} \tag{6}$$

where the sensing matrix $\mathbf{D}$ is the product $\boldsymbol{\Phi}\boldsymbol{\Psi}$, and $\bar{\mathbf{v}}$ is the additive white Gaussian noise (AWGN) vector. The observation vector, $\bar{\mathbf{y}}$, can be also expressed by nonzero elements of $\mathbf{s}$, and their corresponding columns in $\mathbf{D}$, as

$$\bar{\mathbf{y}} = \mathbf{D}_{\mathcal{S}}\,\mathbf{s}_{\mathcal{S}} + \bar{\mathbf{v}} \tag{7}$$

where $\mathcal{S}$ represents the set of the support "locations" of the target pixels. The minimum mean squared estimate of $\mathbf{s}$ is obtained by Masood *et al.,* 2013; Masood, 2015; Masood *et al.,* 2013b.

$$\hat{\mathbf{s}} \triangleq \mathbb{E}[\boldsymbol{s}\,|\bar{\mathbf{y}}] = \sum_{\mathcal{S}\in\mathcal{Z}} p(\mathcal{S}|\bar{\mathbf{y}})\mathbb{E}[\mathbf{s}|\bar{\mathbf{y}},\mathcal{S}] \tag{8}$$

where $\mathcal{Z}$ is a set of all possible sets of nonzero elements of $\mathbf{s}$. Since the distribution of the pixels' values is unknown, finding the conditional expectation, $\mathbb{E}[\mathbf{s}|\bar{\mathbf{y}},\mathcal{S}]$, is impossible. Instead, it is approximated using best linear unbiased estimator given by Masood, 2015:

$$\mathbb{E}[\boldsymbol{s}|\bar{\mathbf{y}},\mathcal{S}] \leftarrow \left[\mathbf{D}_{\mathcal{S}}^{\mathrm{H}}\mathbf{D}_{\mathcal{S}}\right]^{-1}\mathbf{D}_{\mathcal{S}}^{\mathrm{H}}\bar{\mathbf{y}} \tag{9}$$

We use Bayes' rule to break down the conditional probability, $p(\bar{\mathbf{y}},\mathcal{S})$, as

$$p(\mathcal{S}|\bar{\mathbf{y}}) = \frac{p(\bar{\mathbf{y}}|\mathcal{S})p(\mathcal{S})}{p(\bar{\mathbf{y}})} \tag{10}$$

The denominator, $p(\bar{\mathbf{y}})$, is a common factor to all posterior probabilities; hence it is only a scaling factor; therefore it can be ignored. As the target pixels are activated according to Bernoulli's distribution with success probability, say γ, we can write

$$p(\mathcal{S}) = \gamma^{|\mathcal{S}|}(1-\gamma)^{N_x N_y - |\mathcal{S}|} \tag{11}$$

Evaluating the likelihood, $p(\bar{\mathbf{y}}, \mathcal{S})$**,** depends on the distribution of the values of the targets' pixels, which are unknown. However, from (7) we can see that the measurement vector $\bar{\mathbf{y}}$ is composed of two components. The first is a vector in a subspace spanned by the columns of $\mathbf{D}_{\mathcal{S}}$, this vector being of unknown distribution. The second is the noise vector of Gaussian distribution. In the next step, we aim to eliminate the non-Gaussian components of the measurement vector $\bar{\mathbf{y}}$ by projecting $\bar{\mathbf{y}}$ on the orthogonal complement of the matrix $\mathbf{D}_{\mathcal{S}}$ (Masood, 2015), denoted by $\mathbf{D}_{\mathcal{S}}^{\perp}$ and defined as

$$\mathbf{D}_{\mathcal{S}}^{\perp} = \mathbf{I} - \mathbf{D}_{\mathcal{S}}\left[\mathbf{D}_{\mathcal{S}}^{\mathrm{H}}\mathbf{D}_{\mathcal{S}}\right]^{-1}\mathbf{D}_{\mathcal{S}}^{\mathrm{H}} \tag{12}$$

where H is the Hermitian operator. This projection leads to

$$\mathbf{D}_{\mathcal{S}}^{\perp}\bar{\mathbf{y}} = \cancelto{\mathbf{0}}{\mathbf{D}_{\mathcal{S}}^{\perp}\mathbf{D}_{\mathcal{S}}}\mathbf{s} + \mathbf{D}_{\mathcal{S}}^{\perp}\bar{\mathbf{v}} = \mathbf{D}_{\mathcal{S}}^{\perp}\bar{\mathbf{v}} \tag{13}$$

which is a vector of Gaussian distribution with zero mean and covariance matrix given by

$$\mathbf{\Sigma} = \mathbb{E}[(\mathbf{D}_{\mathcal{S}}^{\perp}\mathbf{w}_l)(\mathbf{D}_{\mathcal{S}}^{\perp}\bar{\mathbf{v}})^{\mathrm{H}}] = \mathbf{D}_{\mathcal{S}}^{\perp}\mathbb{E}[\bar{\mathbf{v}}\bar{\mathbf{v}}^{\mathrm{H}}]\mathbf{D}_{\mathcal{S}}^{\perp\,\mathrm{H}} = \sigma_{\bar{\mathbf{v}}}^2\mathbf{D}_{\mathcal{S}}^{\perp}. \tag{14}$$

Now, we can express the likelihood $p(\bar{\mathbf{y}}, \mathcal{S})$ as

$$p(\bar{\mathbf{y}}, \mathcal{S}) \cong \frac{1}{\sqrt{(2\pi\sigma_{\bar{\mathbf{v}}}^2)^M}}\exp\left(-\frac{1}{2}(\mathbf{D}_{\mathcal{S}}^{\perp}\bar{\mathbf{y}})^{\mathrm{H}}\mathbf{\Sigma}^{-1}(\mathbf{D}_{\mathcal{S}}^{\perp}\bar{\mathbf{y}})\right). \tag{15}$$

Now we can find the posterior $p(\mathcal{S}|\bar{\mathbf{y}})$ by substituting (15) and (11) in (10). Hence, we have all essential terms for evaluating the estimate in (8) and find desirable image $\hat{\mathbf{s}}$.

Ideally the summation in (8) should be evaluated over all possible sets in $\mathcal{Z}$, i.e., $2^{N_x N_z}$ possible sets of nonzero pixels, which is computationally expensive. However, given $\mathbf{s}$ to be sparse, we can evaluate the summation over sets for which the posteriors $p(\mathcal{S}, \bar{\mathbf{y}})$ are significant, as expound in next.

A. Finding the Block-Support Sets of the Significant Posteriors

In this section, we demonstrate a greedy algorithm for building a set, $\widehat{\mathcal{Z}}$, which is composed of subsets, $\mathcal{S}_k$, of supports corresponding to significant posteriors $p(\mathcal{S}, \bar{\mathbf{y}})$, i.e., $\widehat{\mathcal{Z}} = \{\mathcal{S}|1 - p(\mathcal{S}, \bar{\mathbf{y}}) < \epsilon\}$ where ϵ is a small number. This set, $\widehat{\mathcal{Z}}$, is then used to replace $\mathcal{Z}$ in (8) and hence it returns the approximate minimum mean square error (AMMSE) estimate of $\mathbf{s}$ as

$$\hat{\mathbf{s}} \cong \mathbb{E}[\boldsymbol{s}\,|\bar{\mathbf{y}}] = \sum_{\mathcal{S}\in\widehat{\mathcal{Z}}} p(\mathcal{S}|\bar{\mathbf{y}})\mathbb{E}[\mathbf{s}|\bar{\mathbf{y}}, \mathcal{S}] \tag{16}$$

Define a selection metric $\nu(\mathcal{S})$ as the logarithmic posterior, then we can write

$$
\begin{aligned}
\nu(\mathcal{S}) &\triangleq \ln\big(p(\mathcal{S}|\bar{\mathbf{y}})\big) \\
&= -\frac{1}{2\sigma_{\bar{\mathbf{v}}}^2}\|\mathbf{D}_{\mathcal{S}}^{\perp}\bar{\mathbf{y}}\|^2 + |\mathcal{S}|\ln\gamma + (N-|\mathcal{S}|)\ln(1-\gamma) \\
&= -\frac{1}{2\sigma_{\bar{\mathbf{v}}}^2}\left\|\mathbf{D}_{\mathcal{S}}\left(\mathbf{D}_{\mathcal{S}}^{\mathrm{H}}\mathbf{D}_{\mathcal{S}}\right)^{-1}\mathbf{D}_{\mathcal{S}}^{H}\bar{\mathbf{y}}\right\|^2 + |\mathcal{S}|\ln\gamma + (N-|\mathcal{S}|)\ln(1-\gamma) \\
&= -\frac{1}{2\sigma_{\bar{\mathbf{v}}}^2}\|\mathbf{D}_{\mathcal{S}}\mathbb{E}[\boldsymbol{s}|\bar{\mathbf{y}},\mathcal{S}]\|^2 + |\mathcal{S}|\ln\gamma + (N-|\mathcal{S}|)\ln(1-\gamma).
\end{aligned}
\tag{17}
$$

The above selection metric is used for building $\widehat{\boldsymbol{\mathcal{Z}}}$ in a sequential greedy manner. The greedy approach starts by evaluating $\nu(\mathcal{S})$ when $\mathcal{S}$ is a single element, i.e., $\mathcal{S} = \{1\},\{2\},\dots,\{N_xN_z\}$. We choose $\mathcal{S}_1 = \mathcal{S}^\star$, where $\mathcal{S}^\star$ is the set of elements corresponding to the maximum value of $\nu(\mathcal{S})$, i.e., $\mathcal{S}^\star \triangleq \arg\max_{\mathcal{S}} \mathrm{p}(\mathcal{S}|\bar{\mathbf{y}})\ \forall\mathcal{S}$. Once $\mathcal{S}^\star$ is chosen, the algorithm searches for the nonzero-pixels in the vicinity of $\mathcal{S}^\star$, where the selection metric is evaluated over $\nu(\mathcal{S}^\star \cup \mathcal{s}^k)$, as $k = 1,2,\dots,K$, for neighbor-pixels of $\mathcal{S}^\star$ as illustrated in Table **1**. We add $\mathcal{S}^k$ to the first selected set, $\mathcal{S}_1$, if the following condition satisfies $\nu(\mathcal{S}^\star \cup \mathcal{s}^k) > \Gamma\nu(\mathcal{S}^\star)$ where $\Gamma = \frac{1}{4}\|\boldsymbol{\psi}\|_2$, and $\boldsymbol{\psi}$ is an arbitrary column in $\boldsymbol{\Psi}$. Then we evaluate $\nu(\mathcal{S})$ for two elements, i.e., $\mathcal{S} = \mathcal{S}_1 \cup \{1\},\{2\},\dots,\{N_xN_z\}$, we choose $\mathcal{S}^\star$ corresponding to the maximum value of $\nu(\mathcal{S})$, along with its neighbors as we did in the previous step. Again, the set $\mathcal{S}_2$ is then constructed such that $\mathcal{S}_2 = \mathcal{S}_1 \cup \mathcal{S}^\star$. This procedure continues in the same manner until $|\widehat{\boldsymbol{\mathcal{Z}}}| = Q$, i.e., $\widehat{\boldsymbol{\mathcal{Z}}} = \{\mathcal{S}_1,\mathcal{S}_2,\dots,\mathcal{S}_Q\}$, where Q is the number of ETs. It should be highlighted that the contribution of this work to the algorithm design is that the elements in the search set $\widehat{\boldsymbol{\mathcal{Z}}}$ are prioritized by their vicinity to the non-zero elements. Additionally, the search for the best $\mathcal{S}_i$ is conducted in dimensions of the image. If the number of the ETs is unknown, the termination criteria are $p(|\widehat{\boldsymbol{\mathcal{Z}}}| > I) \le \beta$, where β is a small number, and I is integer set greater than the expected number of ET as detailed in Table **2**.

Table 1. Finding the contributed pixels of the extended shape of the target in the vicinity of $\mathcal{S}^\star$.

$\mathcal{s}^9$	$\mathcal{s}^{10}$	$\mathcal{s}^{11}$	$\mathcal{s}^{12}$	$\mathcal{s}^{13}$
$\mathcal{s}^K$	$\mathcal{s}^1$	$\mathcal{s}^2$	$\mathcal{s}^3$	$\mathcal{s}^{14}$
$\mathcal{s}^{\vdots}$	$\mathcal{s}^4$	$\mathcal{S}^\star$	$\mathcal{s}^5$	$\mathcal{s}^{15}$
$\mathcal{s}^k$	$\mathcal{s}^6$	$\mathcal{s}^7$	$\mathcal{s}^8$	$\mathcal{s}^{16}$
$\mathcal{s}^{\vdots}$	$\mathcal{s}^{\cdots}$	$\mathcal{s}^{19}$	$\mathcal{s}^{18}$	$\mathcal{s}^{17}$

PERFORMANCE METRICS

To evaluate the quantitative performance, we employ two metrics: Normalized Mean-Squared Error (NMSE) and Earth Mover's Distance (EMD).

The NMSE between the estimated scene, $\check{\boldsymbol{s}}$, and the ground truth, $\boldsymbol{s}$, amounts for the deviation between estimated and the true image vector. Mathematically, it is given by Masood, 2015:

$$
\mathrm{NMSE} = \frac{1}{T}\sum_{t=1}^{T}\frac{\|\check{\boldsymbol{s}}_t - \boldsymbol{s}\|_2^2}{\|\boldsymbol{s}\|_2^2} \tag{18}
$$

where T is the number of Monte Carlo runs for averaging the quantity.

To evaluate the image quality of the reconstructed scene, NMSE alone is not enough as it does not ensure the pixel

locations in the image; thus EMD is defined as a generalized metric. The EMD signifies the level of dissimilarity between distributions and in this context returns the amount of image intensity that has to be moved to convert one image to the other. Lately, EMD became a popular metric for the image comparison (Lagunas, 2014; Leigsnering, 2015).

Inputs arguments: $\bar{\mathbf{y}}$, $\mathbf{D}$, γ.
Initialization: $\mathcal{A} \leftarrow \{1,2,\dots,N_x N_z\}$, $\mathcal{B} \leftarrow \mathcal{A}$, $i = 1, \widehat{\mathcal{Z}} = \phi, \mathcal{N} \leftarrow \{1,2,\dots,K\}, \hat{\mathcal{S}}_0 = \phi$
while $i \leq Q$ **do**
  $\mathcal{C} \leftarrow \{\hat{\mathcal{S}}_{i-1} \cup \{s_1\}, \hat{\mathcal{S}}_{i-1} \cup \{s_2\}, \dots, \hat{\mathcal{S}}_{i-1} \cup \{s_{|\mathcal{B}|}\} | s_j \in \mathcal{B}\}$
  compute $\{v(\hat{\mathcal{S}}_l)\ \forall l, |\hat{\mathcal{S}}_l \in \mathcal{C}\}$ eq. (17)
  find $\mathcal{S}^\star \in \mathcal{C}$ s.t. $v(\mathcal{S}^\star) \geq \max v(\mathcal{S}_l)\ \forall l$
  $\mathcal{S}_i \leftarrow \mathcal{S}^\star$
  for $k = 1$ to 8 **do**
    compute $v(\mathcal{S}^\star \cup s^k)$ eq. (17)
    if $v(\mathcal{S}^\star \cup s^k) > \Gamma v(\mathcal{S}^\star)$
      $\mathcal{S}_i \leftarrow \{\mathcal{S}^\star \cup s^k\}$
    end if
  end for
  $\widehat{\mathcal{Z}} \leftarrow \{\widehat{\mathcal{Z}} \cup \mathcal{S}_i\}$
  $\mathcal{B} \leftarrow \{\mathcal{A} \backslash \mathcal{S}_i\}$
  $i = i + 1$
end while
return $\widehat{\mathcal{Z}}$
compute $\hat{\mathbf{s}}$ eq. (16)

Table 2. Greedy algorithm for building the searching set $\hat{z}$ for Block Bayesian-Based algorithm.

RESULTS AND DISCUSSION

In this section we present results based on MATLAB simulation and experimental data. In the simulation, three scenarios were implemented. The first is an ET with complicated shape, which results into blocks of varying length when the scene is vectorized. The second scenario assumes the Rayleigh distribution of the target pixels. The third scenario simulates the heterogeneous scene containing PTs and ET being reconstructed jointly. For the experimental part, a semi-controlled environment was used to evaluate the performance.

A. Simulated Scenarios

A uniform linear monostatic array composed of 77-elements with aperture length of $2m$ is deployed to capture the image of the scene. The center of the array assumes the system origin. A series of 201 monochromatic waves occupying a spectrum between 1 and 3GHz was employed for the scene interrogation. Only one fourth of the frequency bins and one half of the radar locations were randomly selected to capture the image of the scene where the imaged area was $4 \times 4m^2$. The effect of the front wall is suppressed by spatial filtering as in (Lagunas, 2013). Additive white Gaussian noise with SNR of 20dB was added on the measurement and the reconstructed image is compared with Delay and Sum Beamforming (DSBF) under the same reduced measurement volume. We used the term "conventional CS" as a reference to the algorithm and the model used in (Lagunas, 2014; Leigsnering *et al.*, 2011; Zhang *et al.,* 2015), while the term "Conventional Block CS" refers to the same model in (Lagunas, 2014; Leigsnering *et al.*, 2011) but with Block Orthogonal Matching Pursuit (BOMP) algorithm (Eldar *et al.*, 2010). Since there are various versions of block sparse algorithms, we selected BOMP as it was suggested in TWRI literature as a possible candidate (Lagunas, 2014).

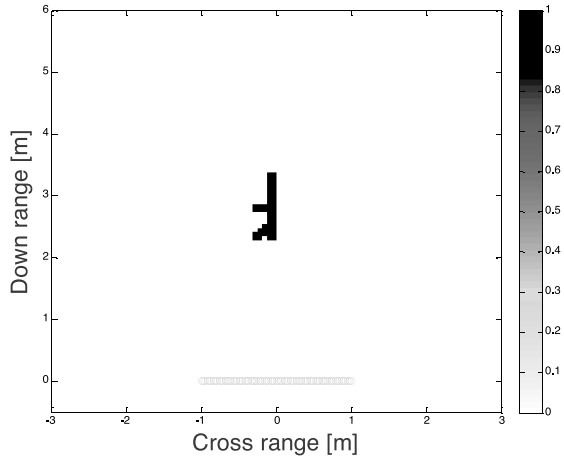

Fig. 2. The original scene with complex shaped target.

Three different scenarios were simulated and the block agnostic approach was compared with selected existing approaches:

A.1. Complex Target with Constant Valued Reflectivity:

In this case, a complex shaped target is simulated as shown in Fig. 2, where the horizontal and vertical axes show the crossrange and the downrange resolutions, respectively, in meters. The blue circles represent the locations where the radar measurements took place, and the color of the pixel indicates the reflection intensity with reference to the color-bar. The image of the scene using the block agnostic is of high quality compared to that of conventional CS and conventional block, BOMP in this case. Fig. 3 (a) shows the reconstructed image using DSBF with reduced data volume, which is highly cluttered due to the point spread function and grating lobes artifacts. The conventional CS, which works under PT assumption, does not well reconstruct the image as depicted in Fig. 3 (b). Also, the BOMP, which works under equal block sizes assumption, fail to correctly reconstruct the complex shaped target for the given data volume as shown in Fig. 3 (c). The relatively poor performance of the conventional equal block sizes assumption is due to the fact that when the scene containing complex shaped target is vectorized, it results into a vector having different block sizes.

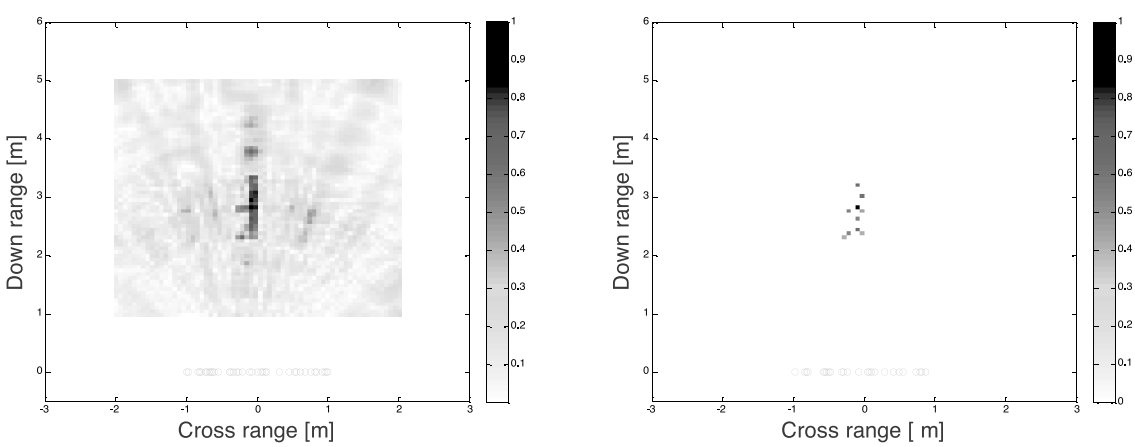

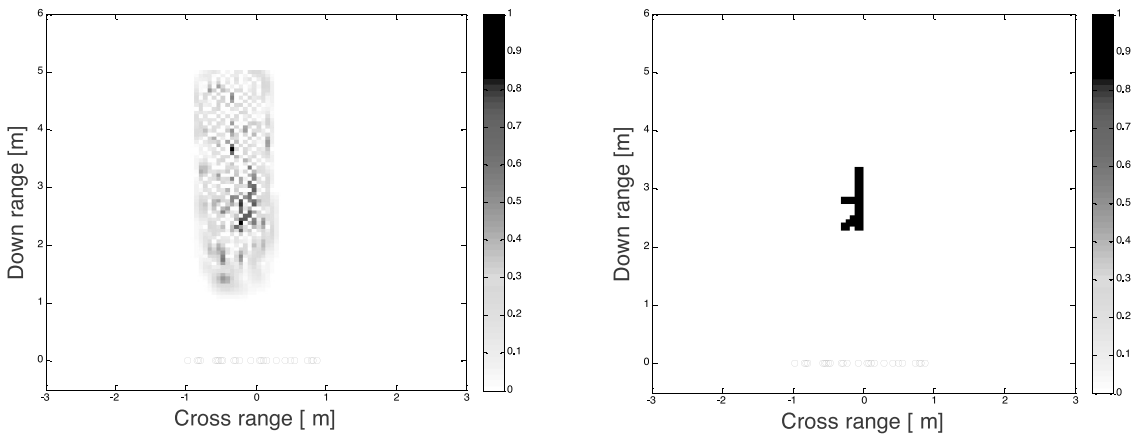

(c) (d)

Fig. 3. Images for uniform target: (a) DSBF; (b) Conventional CS; (c) BOMP; (d) Block Agnostic.

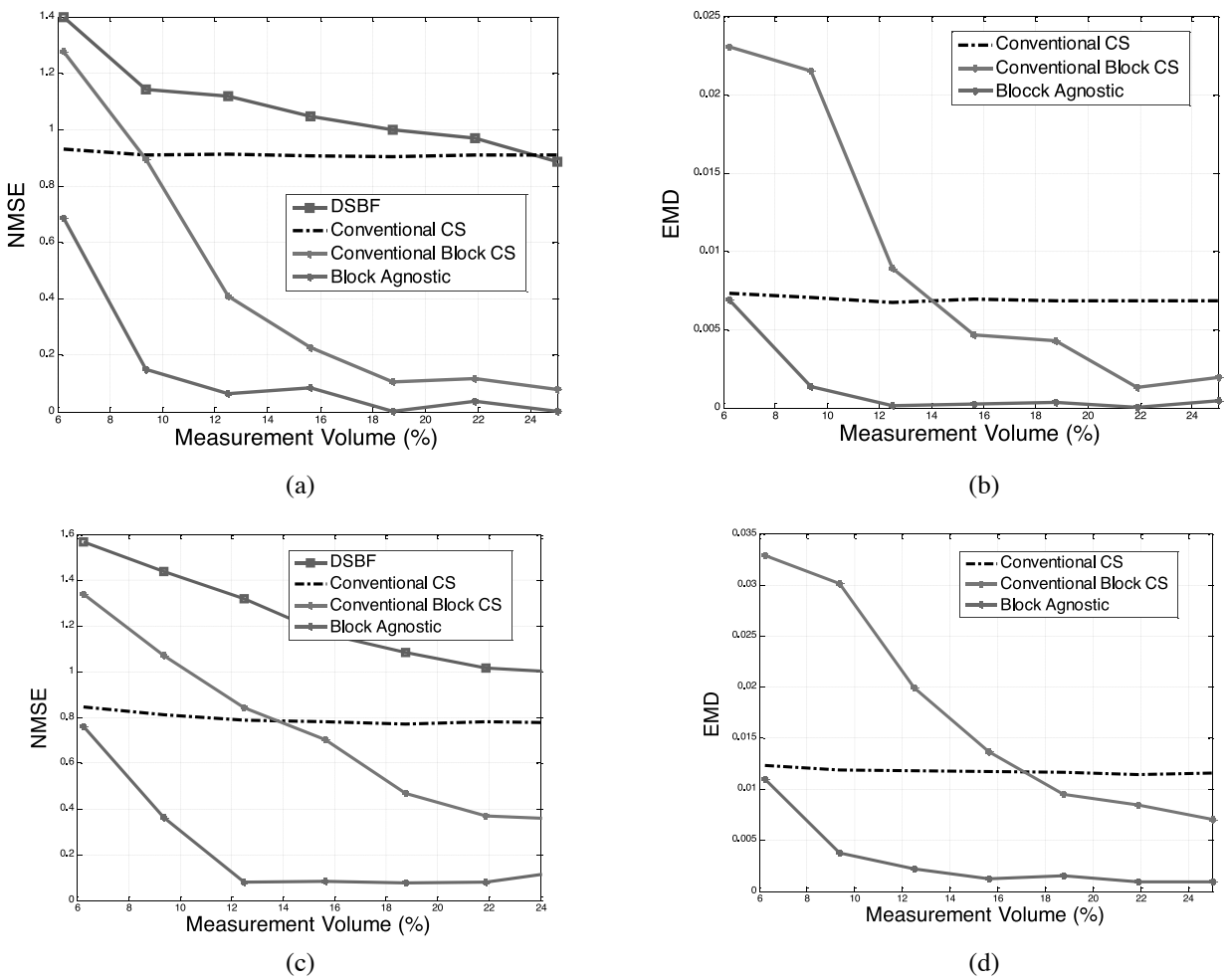

(a) (b)

(c) (d)

Fig. 4. Performance metrics: (a) NMSE for ET with constant reflectivity; (b) EMD for ET with constant reflectivity; (c) NMSE for ET with Rayleigh reflectivity; (d) EMD for ET with Rayleigh reflectivity.

To quantify the performance of the proposed reconstruction approach, NMSE and EMD were evaluated and averaged to 50 Monte Carlo runs. Fig. 4 (a) shows the variation of NMSE with the measurement volume. The DSBF shows the worst performance due to the point spreads function and grating lobes artifacts under equal data volume. The conventional CS shows nearly the same performance as it returns equal number of pixel each time. The block agnostic shows the lowest error, which improves significantly with the increase in data volume. For the EMD, the block agnostic shown in Fig. 4 (b) shows better results and it signifies that the approach ensures both the amplitude and the shape of the target. Due to its relatively poor performance, the DSBF is not shown in the EMD curves.

A.2. Rayleigh Distributed Target Reflectivity:

An ET whose pixel values are drawn from Rayleigh distribution is assumed and the scene to be imaged is shown in Fig. 5. This distribution implies that the deeper the signal traverse, the stronger it gets reflected as in the case of human model. A similar measurement volume to the previous case was used to capture the image. The block agnostic shows a better image quality compared to other simulated methods. As non-agnostic Bayesian based reconstruction algorithms assume Gaussian distribution for the target amplitude, they are not considered here.

Fig. 6 (a) shows the reconstructed image using DSBF with reduced data volume, which is highly cluttered due to the point spread function and grating lobes artifacts. Fig. 6 (b) is the conventional CS, which works under PT assumption, and does not well reconstruct the image, which does not consider the pixel clustering. The reconstructed image using block agnostic algorithm is Fig. 6 (d) outperforms the BOMP because block agnostic algorithm ensures the minimum error. The good performance of block agnostic based method is possibly a result of being independent of the target distribution and the fact that it always minimizes the mean squared error of the estimate.

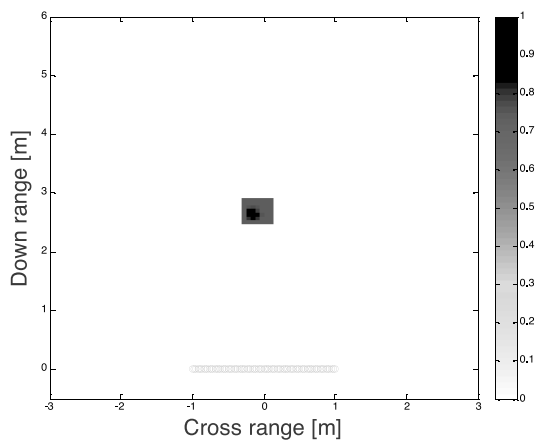

Fig. 5. The scene to be imaged.

The qualitative performance measures, NMSE and EMD, support the image qualities shown in Fig. 4 (c), which shows the variation of NMSE with measurement volume for different reconstruction approaches and the block agnostic shows good performance due to the fact that it always ensures the minimum error. Fig. 6 (d) is the variation of EMD with data volume with DSBF excluded due to its worst case performance. Overall, the block agnostic approach shows better performance for both metrics.

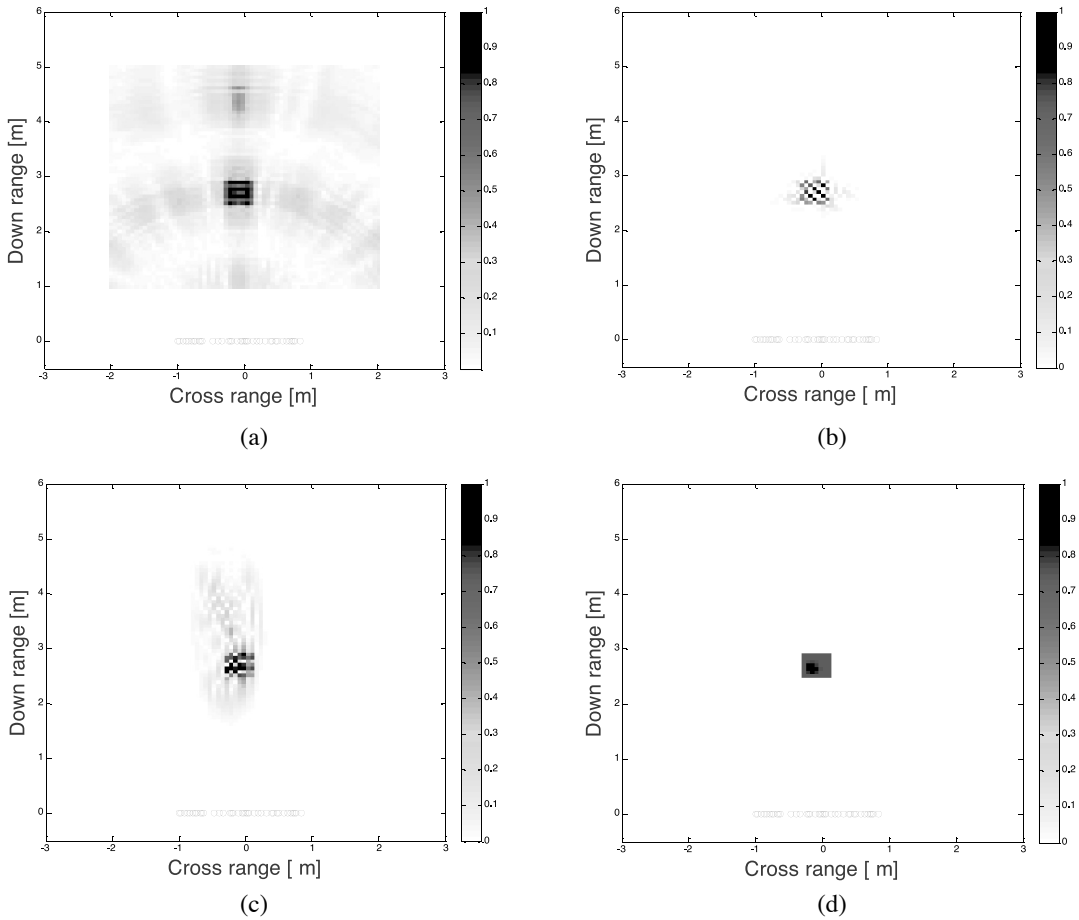

Fig. 6. Images for Rayleigh Target: (a) DSBF; (b) Conventional CS; (c) BOMP; (d) Block Agnostic.

A.3. Joint ET and PT Reconstruction:

Another advantage of the proposed reconstruction approach, block agnostic, is its ability to jointly reconstruct PTs and ETs by treating PTs as blocks of single pixel contrary to the previous approaches where the two are reconstructed separately. Consider a ground truth shown in Fig. 7 containing both PTs and ET.

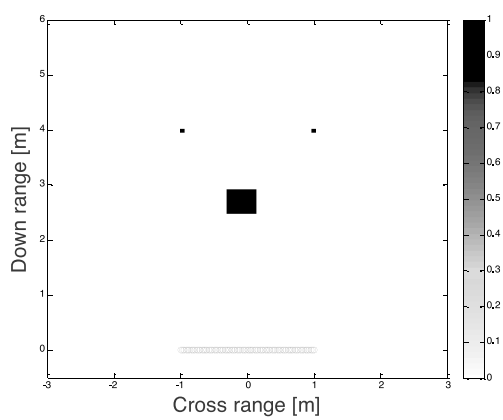

Fig. 7. Original scene containing PT and ET.

The same amount of reduced data volume was used to capture the image of the scene and the block agnostic yield the best image quality as shown in Fig. 8. Fig. 8 (a) is the image reconstructed using DSBF and Fig. **8** (b) is the image using conventional CS approach. Fig. 8 (c) is the image using conventional block approach and Fig. 8 (d) represents the image using the block agnostic.

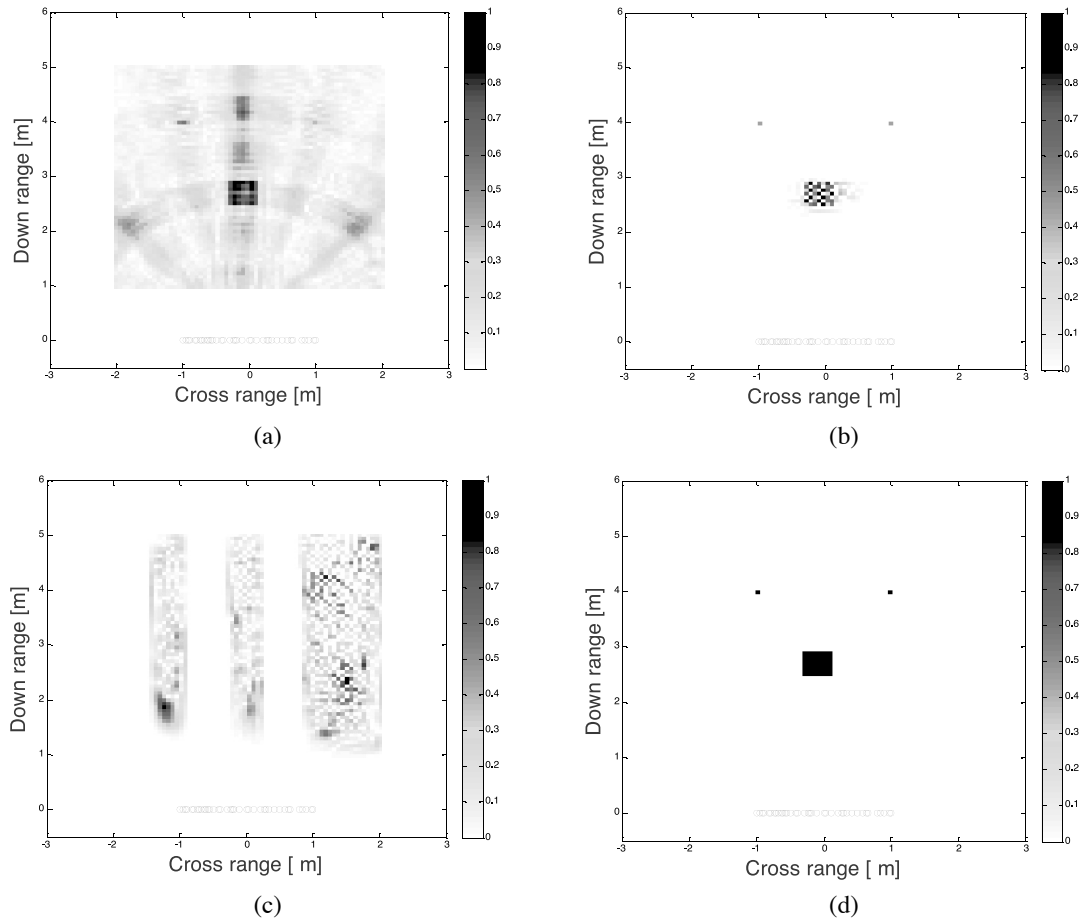

Fig. 8. Images for ET-PT joint reconstruction: (a) DSBF; (b) Conventional CS; (c) BOMP; (d) Block Agnostic.

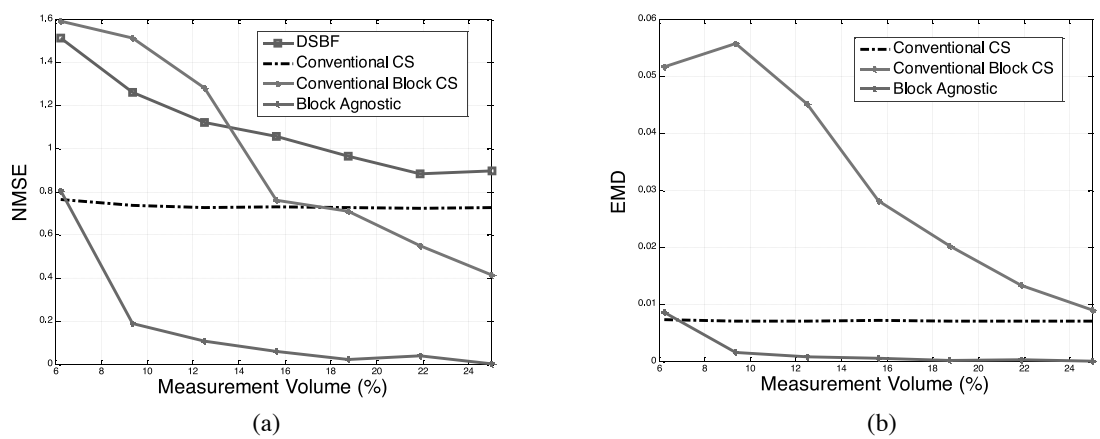

Fig. 9. Performance metrics for joint ET-PT reconstruction with data volume: (a) NMSE; (b) EMD.

The variations of NMSE and EMD are shown in Fig. 9 (a) and (b), respectively, for different data volumes. Both metrics favor the block agnostic approach. The EMD curve for DSBF shows relatively low performance and it is not shown for clarity. The curves suggest that the performance can be further improved with expense of increasing data volume.

1. B. Experimental Results

An experiment was conducted in the Electrical Engineering department's building, King Fahd University of Minerals and Petroleum. The setup involved two cylindrical targets of radius $23cm$ located at $(-0.75,2)m$ and $(0.5,3)m$ as shown in Fig. 10. Measurement of the background was first captured to suppress front wall reflections and other clutters. Only 12.5% of the measurement volume was used to reconstruct the sparse images using conventional CS, BOMP, and block agnostic algorithms.

Fig. 11 (a) shows the image formed using DSBF with full data volume, which is used as benchmark; Fig. 11(b) shows the image reconstructed with conventional CS while assuming PT model. In this case, the algorithm does not take into account the target extent and, therefore, could not recover the shape of the target. Fig. 11 (c) shows the image reconstructed using BOMP giving unsatisfactory results possibly due to the size of the data volume. The block agnostic algorithm, on the other hand, gives more information about the target extent as shown in Fig. 11 (d).

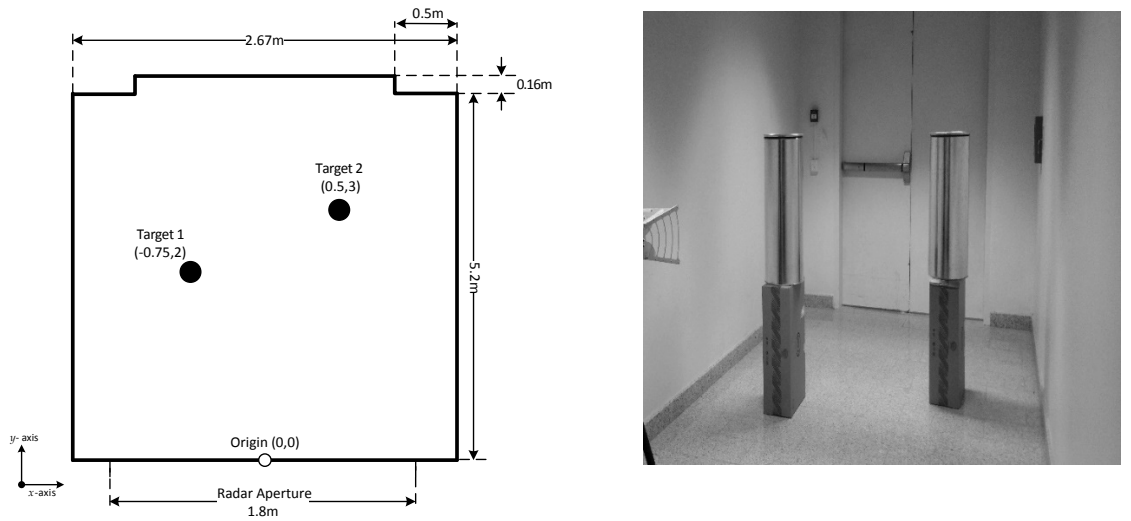

(a) (b)

Fig. 10. The scene: (a) room layout; (b) experimental setup.

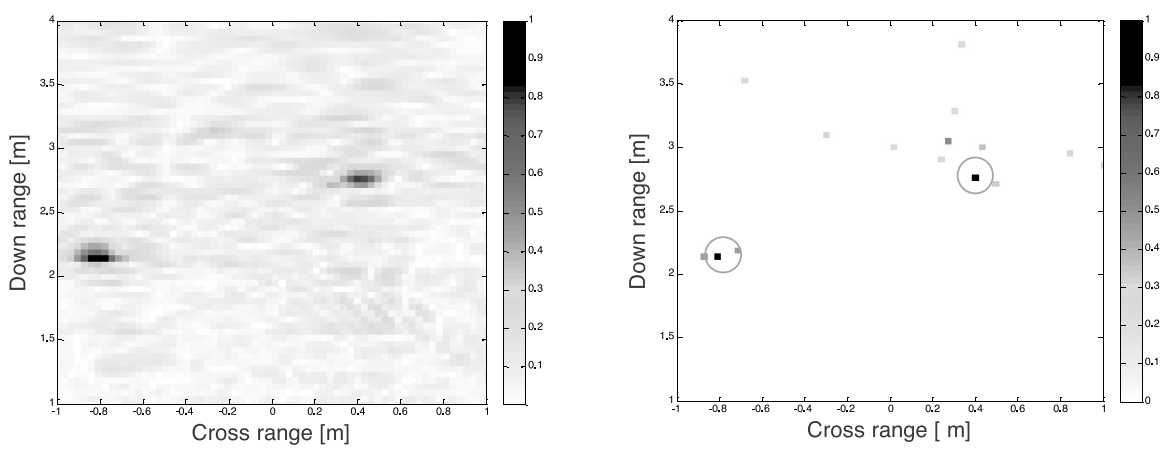

(a) (b)

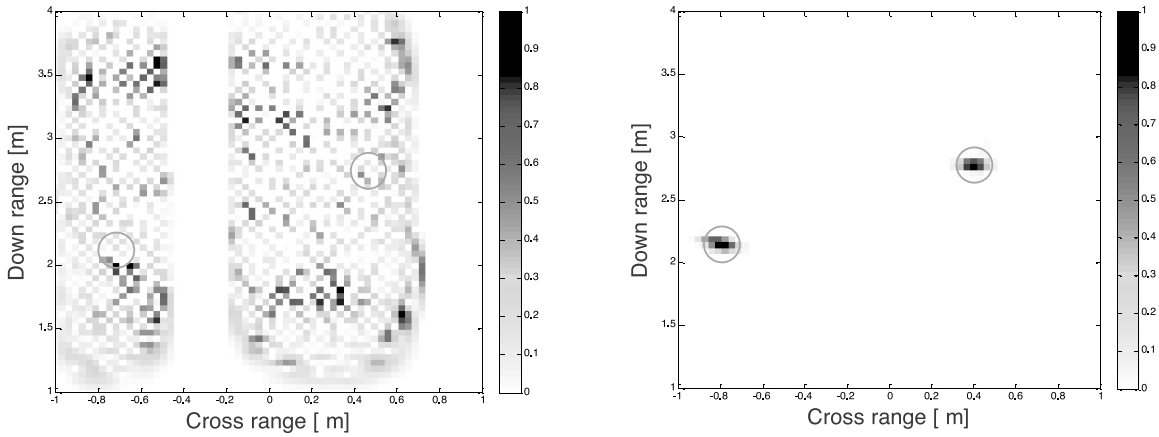

(c) (d)

Fig. 11: Images: (a) DSBF; (b) conventional CS; (c) Conventional block sparse reconstruction; (d) Block Agnostic.

CONCLUSIONS

In this paper, a new reconstruction algorithm for ETs is suggested based on block agnostic algorithm with varying block sizes. The overall ground truth is considered as a sum of disjoint ground truths with different target sizes, shapes and following different probability distributions. The model best reflects the TWRI scenarios where the expected targets may possess complex shapes, which when vectorized by concatenating the columns of the discretized version of the ground truth results in a vector with different block sizes. This feature enables the concurrent reconstruction of PTs and ETs by treating PTs as blocks with only one pixel. Further, the model assumes that the distributions of the reflectivity values for the corresponding targets are not necessarily known. This is because in multiple and independent target scenario, considering the target being a human with rifle, the resulting image vector comprises chunks of pixels. Each chunk is drawn from different distributions making the overall pixel distribution intractable. Among other attractive features of the block agnostic recovery is the fact that it reconstructs the scene using minimum mean squared error estimator. Both qualitative and quantitative results based on MATLAB simulations and experimental data show the effectiveness of the block agnostic based approach. However, the size of the target influences the overall performance as it lowers the sparsity of the scene.

As the extension of this work, the effect of multipath can be studied and also an appropriate multipath ghost suppression scheme can be suggested.

ACKNOWLEDGMENT

This work is funded by the National Plan for Science, Technology and Innovation (Maarifah), King Abdul Aziz City for Technology, through the Science and Technology Unit at King Fahd University of Petroleum and Minerals (KFUPM), The Kingdom of Saudi Arabia, award number 15-ELE4651-04. The author would like to acknowledge the help provided by undergraduate and graduate students in performing experiments and data collection.

REFERENCES

Abdalla, A.T. & Muqaibel, A. H. 2015. Multiple Target Sparse Reconstruction in TWRI Utilizing Ghost's Aspect Dependence Feature. Proceedings of the *IEEE International RF and Microwave Conference*. Kuching, Malaysia.

Alkhodary, M.T. & Muqaibel, A. H. 2017. Efficient grouping technique for low mutual-coherence basis matrix in radar imaging. *Electronics Letters*, *53*.

Alkhodary, M.T. & Muqaibel, A.H. 2018. Low complexity sparse Bayesian estimation for UWB radar imaging. *IET Radar, Sonar and Navigation*, *12*.

Amin, M.G. & Ahmad, F. 2013. Compressive sensing for through-the-wall radar imaging. *Journal of Electronic Imaging*, *22*.

Eldar, Y.C., Kuppinger, P. & Bolcskei, H. 2010. Block-Sparse Signals: Uncertainty Relations and Efficient Recovery. *IEEE Transactions on Signal Processing*, *58*.

Gennarelli, G., Vivone, G., Braca, P., Soldovieri, F. & Amin, M.G. 2015. Multiple Extended Target Tracking for Through-Wall Radars. *IEEE Transactions on Geoscience and Remote Sensing*, *53*.

Gurbuz, A.C., McClellan, J.H. & Scott, W.R. 2009. A compressive sensing data acquisition and imaging method for stepped frequency GPRs. *IEEE Transactions on Signal Processing*, *57*.

Huang, Q., Qu, L., Wu, B. & Fang, G. 2010. UWB through-wall imaging based on compressive sensing. *IEEE Transactions on Geoscience and Remote Sensing*, *48*.

Lagunas, E. 2014. Compressive Sensing Based Candidate Detector and its Applications to Spectrum Sensing and Through-the-Wall Radar Imaging.

Lagunas, E., Amin, M.G., Ahmad, F. & Nájar, M. 2013. Wall mitigation techniques for indoor sensing within the compressive sensing framework. *IEEE Trans. Geosci. Remote Sens*, *51*.

Leigsnering, M. 2015. *Sparsity-Based Multipath Exploitation for Through-the-Wall Radar Imaging*. Ph.D. thesis der Technischen Universitat Darmstadt, Darmstadt, Germany.

Leigsnering, M., Debes, C. & Zoubir, A. M. 2011. Compressive Sensing in Through-The-Wall Radar Imaging. Proceedings of the IEEE Int. Conf. Acoustics, Speech and Signal Processing, Prague, Czech Republic.

Liu, B., Zhang, Z., Fan, H. & Fu, Q. 2012. Fast Marginalized Block Sparse Bayesian Learning Algorithm, *X*, technical report, https://arxiv.org/abs/1211.4909.

Masood, M. 2015. *Distribution Agnostic Structured Sparsity Recovery: Algorithms and Applications*. Ph.D. thesis, King Abdullah University of Science and Technology, Thuwal Saudi Arabia.

Masood, M. & Al-Naffouri, T.Y. 2013. Sparse Reconstruction Using Distribution Agnostic Bayesian Matching Pursuit. Signal Processing, IEEE Transactions, 61.

Masood, M. & Al-Naffouri, T.Y. (2013a). Sparse reconstruction using distribution agnostic Bayesian matching pursuit. IEEE Transactions on Signal Processing, 61.

Masood, M. & Al-Naffouri, T.Y. 2013b. Support agnostic Bayesian matching pursuit for block sparse signals. Proceedings of the ICASSP, IEEE International Conference on Acoustics, Speech and Signal Processing - Proceedings.

Muqaibel, A.H., Abdalla, A.T., Alkhodary, M. T. & Al-Dharrab, S. 2017. Aspect-dependent efficient multipath ghost suppression in TWRI with sparse reconstruction. International Journal of Microwave and Wireless Technologies.

Muqaibel, A. H., Abdalla, A. T., Alkhodary, M. T. & Alawsh, S.A. 2017. Through-the-wall radar imaging exploiting Pythagorean apertures with sparse reconstruction. Digital Signal Processing: A Review Journal, 61.

Nicolaescu, I., van Genderen, P., Van Dongen, K.W., van Heijenoort, J. & Hakkaart, P. 2003. Stepped frequency continuous wave radar-data preprocessing. In Proceedings of the 2nd International Workshop on Advanced Ground Penetrating Radar.

Sun, H., Yu, L., Jia, J. & Wei, C. 2016. Compressive sensing for cluster structured sparse signals: variational Bayes approach. IET Signal Processing, 10.

Wu, Q., Zhang, Y.D., Amin, M.G. & Himed, B. 2015. Multi-task Bayesian compressive sensing exploiting intra-task dependency. IEEE Signal Processing Letters, 22.

Wu, Q., Zhang, Y. D., Amin, M. G., Himed, B., Ahmad, F. & Amin, M. G. 2015. Compressive-sensing-based high-resolution polarimetric through-the-wall radar imaging exploiting target characteristics. IEEE Antennas and Wireless Propagation Letters, 14.

Yoon Y.S. & Amin, M.G. 2008. High resolution through-the-wall radar imaging using extended target model. Proceedings of the Radar Conference, RADAR.

Zhang, Z. & Rao, B. D. 2012. Recovery of block sparse signals using the framework of block sparse Bayesian learning. Proceedings of the 2012 IEEE International Conference on Acoustics, Speech and Signal Processing.

Submitted: 19/11/2017
Revised: 05/02/2019
Accepted: 05/02/2019

نمذجة الأجسام الممتدة وبناء الصورة الراديوية لها عبر الجدار: منظور مختلف

عبدي طالب عبد الله، **محمد تميم الخضري و علي حسين مقيبل**
*قسم الهندسة الإلكترونية والاتصالات السلكية واللاسلكية، جامعة دار السلام، دار السلام، تنزانيا
**قسم الهندسة الكهربائية، مدرسة التكنولوجيا العليا، مونتريال، كندا.
***قسم الهندسة الكهربائية، جامعة الملك فهد للبترول والمعادن، الظهران، المملكة العربية السعودية

الخلاصة

إن ما اعتاد عليه الباحثون في مجال التصوير الراديوي لما خلف الجدار (TWRI) هو افتراض أن الأجسام المستهدفة في التصوير لا يتجاوز حجمها نقطة واحدة (PT) في الصورة الراديوية النهائية. إلا أن الواقع العملي يختلف عن هذا الافتراض في كثير من الأحيان؛ وذلك أن بعض الأجسام يتجاوز حجمها النقطة في الصورة النهائية وهو ما نطلق عليه في بحثنا هذا: الجسم الممتد. إن التصوير الراديوي عالي الدقة بحاجة إلى نمذجة عامة لمثل هذه الأجسام الممتدة، ولذلك فإننا نقترح طريقة لنمذجة الأجسام الممتدة وكذلك طريقة لبناء الصورة الراديوية لها بخوارزمية لا تعتمد على المعلومات الإحصائية لهذه الأجسام، وإنما تستفيد من الخاصية المتناثرة لهذه الأجسام في الصورة. كذلك فإن الخوارزمية لا تتطلب أي معلومات عن مدى امتداد الأجسام أو عددها أو توزيعها الاحصائي. تظهر النتائج المستندة إلى محاكاة برنامج ماتلاب MATLAB والبيانات التجريبية فعالية النموذج المقترح والخوارزمية لبناء الصور الراديوية النهائية. إن التطبيقات الخوارزمية المقترحة ذات أهمية في قطاعات الدفاع المدني والإنقاذ والمراقبة والأمن، حيث يعد التتبع الدقيق للأهداف الكبيرة خلف الجدران أمراً حيوياً.